Scattering-Aware Color Calibration for 3D Printers Using a Simple Calibration Target

TOMÁŠ ISER, Charles University, Czech Republic and Additive Appearance, Czech Republic
TOBIAS RITTIG, Additive Appearance, Czech Republic
ALEXANDER WILKIE, Charles University, Czech Republic and Additive Appearance, Czech Republic

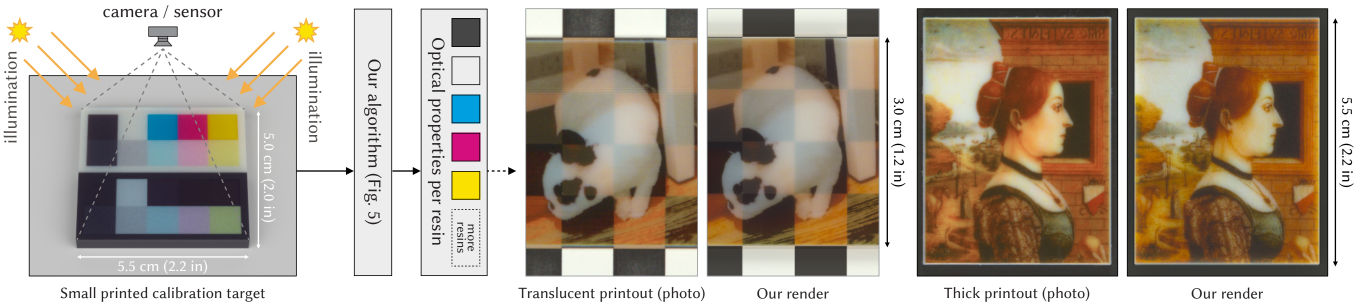

Fig. 1. We designed a small calibration target (left), where thin, translucent resin layers are stacked on top of thick black and white layers. The target is 3D printed, illuminated, and captured using a camera, or optionally a spectrometer if spectral accuracy is desired. The color of each patch is processed in our algorithm (Fig. 5), outputting the physical optical properties (single-scattering albedo and extinction coefficient) for each resin. The properties are used for accurate predictions of 3D printouts' appearances, which is also useful for scattering-aware halftoning optimization loops (Fig. 2).

We present a novel method for accurately calibrating the optical properties of full-color 3D printers using only a single, directly printable calibration target. Our approach is based on accurate multiple-scattering light transport and estimates the single-scattering albedo and extinction coefficient for each resin. These parameters are essential for both soft-proof rendering of 3D printouts and for advanced, scattering-aware 3D halftoning algorithms. In contrast to previous methods that rely on thin, precisely fabricated resin samples and labor-intensive manual processing, our technique achieves higher accuracy with significantly less effort. Our calibration target is specifically designed to enable algorithmic recovery of each resin's optical properties through a series of one-dimensional and two-dimensional numerical optimizations, applied first on the white and black resins, and then on any remaining resins. The method supports both RGB and spectral calibration, depending on whether a camera or spectrometer is used to capture the calibration target. It also scales linearly with the number of resins, making it well-suited for modern multi-material printers. We validate our approach extensively, first on synthetic and then on real resins across 242 color mixtures, printed thin translucent samples, printed surface textures, and fully textured 3D models with complex geometry, including an eye model and a figurine.

CCS Concepts: • **Computing methodologies** → **Rendering**; *Reflectance modeling*; • **Applied computing** → **Computer-aided manufacturing**.

Authors' Contact Information: Tomáš Iser, tomas@cgg.mff.cuni.cz, Charles University, Prague, Czech Republic and Additive Appearance, Prague, Czech Republic; Tobias Rittig, tr@appearan.cz, Additive Appearance, Prague, Czech Republic; Alexander Wilkie, wilkie@cgg.mff.cuni.cz, Charles University, Prague, Czech Republic and Additive Appearance, Prague, Czech Republic.

ACM 1557-7368/2025/12-ART182
https://doi.org/10.1145/3763293

Additional Key Words and Phrases: color calibration, 3D printing, resins, optical properties, translucency measurement, volumetric scattering, volumetric absorption, subsurface scattering, computational fabrication, predictive rendering, radiative transport, adding doubling

ACM Reference Format:
Tomáš Iser, Tobias Rittig, and Alexander Wilkie. 2025. Scattering-Aware Color Calibration for 3D Printers Using a Simple Calibration Target. *ACM Trans. Graph.* 44, 6, Article 182 (December 2025), 14 pages. https://doi.org/10.1145/3763293

1 Introduction

Material-jetting 3D printers equipped with colored resins can create printouts with an intricate, textured appearance [Bader et al. 2018] (see Fig. 1). Their inkjet printheads deposit liquid resins next to each other, where the resins are different primary colors, typically cyan, magenta, yellow, black, and white (CMYKW). Each layer is solidified with ultraviolet (UV) light in a photopolymerization process and by stacking layers an arbitrary 3D shape can be formed.

A single resin droplet is typically in the order of tens of micrometers, so 1 cm^3 consists of millions of droplets arranged in a 3D grid. The printing process is discrete, meaning that each coordinate corresponds to exactly one resin and they are idealized as having no droplet mixing. However, because the resin droplets are translucent, they scatter and selectively absorb photons beneath the surface, causing visual color mixing within the printout and acting as a blur filter. Even a single voxel deep inside the object can influence the surface appearance. Brunton et al. [2015] demonstrated that this is a challenging scenario, more difficult than in 2D printing.

A challenging problem is how to arrange resins in the 3D grid to achieve a given appearance (texture). Many algorithms have been presented (Sec. 2) where some can even counteract the blur and loss

Table 1. The notation of physical quantities used throughout this publication, including their meaningful ranges, units, and relations.

Symbol	Range	Unit	Description	Useful relations
σ_a	$[0, \infty)$	mm^{-1}	*Absorption coefficient*; $\exp(-\ell \cdot \sigma_a)$ is the fraction of collimated light absorbed in a homogeneous layer of σ_a over ℓ mm of distance	$\sigma_a = (1-\alpha) \cdot \sigma_t = \sigma_t - \sigma_s$
σ_s	$[0, \infty)$	mm^{-1}	*Scattering coefficient*; $\exp(-\ell \cdot \sigma_s)$ is the fraction scattered out	$\sigma_s = \alpha \cdot \sigma_t = \sigma_t - \sigma_a$
σ_t	$[0, \infty)$	mm^{-1}	*Extinction coefficient*; $\exp(-\ell \cdot \sigma_t) = \exp(-\ell \cdot \sigma_a) \cdot \exp(-\ell \cdot \sigma_s)$	$\sigma_t = \sigma_a + \sigma_s = \tau / \ell$
α	$[0, 1]$	-	Single-scattering *albedo*; a ratio of scattering to extinction	$\alpha = \sigma_s / \sigma_t$
ℓ	$[0, \infty)$	mm	Physical thickness of a homogeneous layer	$\ell = \tau / \sigma_t$
τ	$[0, \infty)$	-	Optical thickness of a homogeneous layer	$\tau = \ell \cdot \sigma_t$

of contrast caused by lateral subsurface light transport [Elek et al. 2017; Nindel et al. 2021; Sumin et al. 2019]. These approaches are based on iterative optimization loops (Fig. 2), that utilize predictions of the surface appearance to fine-tune the arrangement.

Typically, this prediction relies on Monte Carlo volumetric path tracing, which requires the resins' optical properties, some of which are summarized in Table 1 (consider also Jarosz [2008] or Novák et al. [2018] for an overview). Although Monte Carlo path tracing was also demonstrated for non-exponential, spatially-correlated media [Bitterli et al. 2018; Jarabo et al. 2018], the general assumption that we also follow in this publication is that light absorption and scattering are exponential effects. Each resin is then optically characterized by its *extinction coefficient* σ_t $\left[\mathrm{mm}^{-1}\right]$, the *single-scattering albedo* α, the *index of refraction* η, and the *phase function* describing the angular distribution of light scattering. Each of these parameters is RGB or wavelength-dependent.

Previous measurement literature [e.g., Elek et al. 2017, 2021; Kissel et al. 2025] showed that for 3D printing resins, we can reasonably assume a refractive index $\eta \approx 1.5$ and the Henyey and Greenstein [1941] phase function with $g \approx 0.4$, although our method conceptually works with other phase function parameters as well, which follows from similarity relations [Wyman et al. 1989; Zhao et al. 2014] and we also demonstrate it later in one of our experiments. We therefore set these parameters constant and focus on calibrating the unknown α and σ_t of each resin, both in RGB and spectrally.

Calibrating the resins effortlessly is important. Manufacturers often release new resins with improved performance but different optical properties (e.g., Stratasys Vero, VeroVivid, VeroUltra, TrueDent, Agilus30 Colors, VeroEco Flex, which are all families of differently colored resins). Different batches of the same family printed on various printers also result in slightly different properties [Kissel et al. 2025]. In the face of a growing number of printheads per machine and research printers with open material ecosystems, traditional one-time calibrations that rely on combinatorics are becoming unsuitable [Song et al. 2018]. Users may also want to print with custom resins to increase the color gamut [Shi et al. 2018]. Unfortunately, existing calibration methods for individual resins require manual preparation and careful polishing of thin resin samples [Elek et al. 2021; Iser et al. 2022; Song et al. 2016], or require precise calibrations and expensive laboratory equipment, such as integrating spheres [Kissel et al. 2025; Song et al. 2018, 2016].

Our contribution. In this paper, we present a new calibration strategy that does not require any laboratory equipment, and is based on a single, simple and compact calibration target. The target can be 3D printed and measured in-situ on the machine whose calibration is performed, which is a significant improvement over previous methods that required manual interaction. Our method is compatible with any set of at least two resins, with the only requirement being that two of them have a high contrast, which is a natural expectation in full-color printing with black and white. The runtime and target size scale linearly with the number of resins, so it is suitable even for printing with a large number of resins, e.g., for spot colors. Our algorithm is based on three principles (Fig. 5), which we derived from observing how optical reflectance depends on α and σ_t in semi-infinite, layered samples. We demonstrate that there are one-to-one mappings between reflectance and the optical properties under certain assumptions and that a series of one-dimensional and two-dimensional algorithmic space searches suffice to find the properties within a couple of minutes. To evaluate the method, we first design a synthetic experiment as a proof of concept. Finally, we extensively evaluate the calibration on real resins and 3D printed color mixtures, thin translucent samples, textures on slabs, and textured 3D models. We also compare our results to other publications.

2 Related work

Our calibration method lies at the boundary of two fields in computer graphics. First, full-color 3D printing and appearance fabrication (Sec. 2.1; see also the review of Yuan et al. [2021]). And second, measurement methods for estimating α and σ_t of translucent materials (Sec. 2.2). Note that additional information on obtaining optical properties of translucent materials in general, beyond the 3D printing scope, can be found in the survey of Frisvad et al. [2020].

2.1 Full-color 3D printing and appearance fabrication

Initially, fabrication papers in graphics focused on subsurface scattering without color calibrations [Dong et al. 2010; Hašan et al. 2010]. The first full-color method was presented by Brunton et al. [2015]. They printed and measured a large calibration target with 512 combinations of CMY resins on top of a white resin slab, from which they constructed a CMY↔RGB lookup table. To print a 3D texture, the lookup table was used together with *halftoning* based on 3D error diffusion. Although the method was later extended to support transparency and alpha-channel printing [Brunton et al. 2018; Urban et al. 2019], subsurface scattering was not taken into account.

Babaei et al. [2017] presented *contoning* (stacking resins on top of each other) as an alternative to halftoning to improve the visual

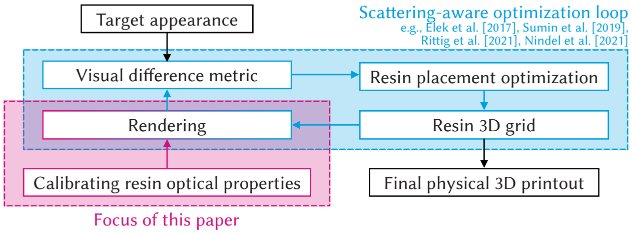

Fig. 2. Diagram of scattering-aware optimizations for halftoning full-color 3D printouts. We propose a new optical calibration method and evaluate it for rendering, which is a necessary component of the pipeline.

quality. They used a modified model of Kubelka and Munk [1931] [Nobbs 1985], taking into account an entire stack of resin layers up to a certain thickness. Simulating the appearance of resin layers and/or the local neighborhood is also possible using *deep neural networks* trained on calibration targets of varying resin arrangements [Chen and Urban 2021; Nagasawa et al. 2022, 2021; Shi et al. 2018]. An orthogonal line of work is concerned with *gloss*, i.e. the specularity of surface reflectance mostly achieved using transparent ink or varnish; focusing on its capture [Elkhuizen et al. 2020], calibrated fabrication [Piovarči et al. 2020], and perceptual impact on the appearance [Condor et al. 2023]. Recently, directional reflectance also became of interest in 2.5D [Habib et al. 2023] and 3D printing [Abu Rmaileh and Brunton 2023].

The most complex methods use accurate volumetric rendering with subsurface scattering. In an *iterative optimization loop* (Fig. 2), resins are first distributed on the surface, the printout is rendered, and the visual error between the prediction and target appearance is used in the next iteration to improve the resin arrangement. This results in detailed, high-contrast printouts that are unachievable with other methods. It was first presented by Elek et al. [2017] on planar slabs and later extended for full 3D geometries with thin features [Sumin et al. 2019]. Follow-up works used Radiance-Predicting Neural Networks (RPNNs) to improve the performance of the rendering step [Rittig et al. 2021] or formulated the whole optimization problem in a differentiable rendering context [Nindel et al. 2021]. Using differentiable rendering, Luci et al. [2024] fit the optical properties of the resins and infer a mixing pattern between neighboring voxels. In this paper, we focus on calibrating the optical properties for each resin, which extends the viability of these previously-mentioned works that build on accurate rendering.

2.2 Estimating the α and σ_t scattering properties

In physics, scattering properties are typically estimated from the total *hemispherical reflectance and transmittance* of a material sample [Pickering et al. 1992, 1993; Prahl et al. 1993] using two integrating spheres or a Coblentz hemisphere [Schröder et al. 2015]. Recent works focused on setups with a single integrating sphere [Terán et al. 2019] and creating an optimized measurement system, improving the accuracy with Monte Carlo simulations, and taking the exact sphere geometry into account [Bergmann et al. 2020; Foschum et al. 2020]. The fitting of the properties (α, σ_t, and optionally g) to measured quantities can be done using *inverse adding doubling* [Prahl 2011], a diffuse four-flux model [Song et al. 2018, 2016], or Monte Carlo simulations. In the context of 3D printing, the integrating sphere setup was demonstrated by Kissel et al. [2025], which we included in one of our comparisons (Sec. 6.7). Their high accuracy comes at the cost of expensive laboratory equipment and the need for manual preparation of thin resin samples. In our method, the calibration target can be 3D printed and photographed as-is.

In search of low-cost setups, methods based on *lateral scattering profiles* emerged. A sample is photographed and the falloff profile of the reflected light is analyzed. Examples include the dilution method [Narasimhan et al. 2006], diffusion-based prediction models [Jensen et al. 2001; Weyrich et al. 2006], or a combination of Monte Carlo and quantized diffusion [D'Eon and Irving 2011; Papas et al. 2013]. Closest to our work, Kienle et al. [1998] fit the properties of a two-layer stack from the falloff of an orthogonal laser beam and swapping the layer order, which is related to our Principle 2 (Sec. 3.3). Elek et al. [2021] measured 3D printing resins from the lateral scattering profile of thin resin samples on a black and white step edge. There are two downsides: first, modern color resins have a high σ_t, requiring extremely thin samples with a consistent thickness and a well-polished surface. Second, the capture relies on a one-dimensional signal (lateral light spread), so it can only be captured by a camera and not a point spectrometer. Accuracy issues may arise in RGB calibrations, as we show in Fig. 10 [consider also the supplemental document of Iser et al. 2022].

The latter downside was solved by Iser et al. [2022], who showed that two spot measurements on separate black and white backgrounds, and an optional transmission measurement, are sufficient. Pranovich et al. [2024] modified the approach by only approximating single scattering to avoid the slow pre-computations. Both require manually prepared samples of various thicknesses to ensure a robust fit. One of the strongest downsides of methods based on thin samples is the difficulty in preparing very thin, polished resin samples, which makes it hard to predict highly absorbing resins. Later in our evaluation experiments, we show that our method outperforms Iser et al., especially on the strongly absorptive yellow resin, even when using an RGB camera instead of a spectrometer. Difficulties with the yellow resin were also observed in the concurrent work of Abu Rmaileh et al. [2025], who use Monte Carlo simulations of resin samples to train a machine learning model. Their method also allows determining the intrinsic optical properties of the resins. As the method was published just after our original submission deadline, we were unable to provide a direct comparison.

Certain methods can also estimate the phase function anisotropy g, which is assumed to be fixed in our method. While Pranovich et al. [2024] assumed $g = 0.0$ (isotropic), others showed that most resins are forward scattering with $g \approx 0.4$ [Elek et al. 2021; Kissel et al. 2025] or $g \in [0.0, 0.8]$ [Iser et al. 2022]. In practice, small errors in g should simply result in scaled σ_s as described by similarity relations [Wyman et al. 1989; Zhao et al. 2014] under the assumption of semi-infite media. Precise phase function estimations are possible by measuring the out-scattering of a collimated beam from various angles using laboratory equipment [Gkioulekas et al. 2013; Leyre et al. 2014], or, for optically-thin or dilluted media, capturing a diffused image of the single-scattering field [Minetomo et al. 2018].

3 Method

We assume a *flat, plane-parallel geometry* (Fig. 3) for which one-dimensional light transport can be described by accurate *adding-doubling equations* that model multiple scattering in layered materials (Sec. 3.1). Using these equations, we study the relations between the reflectance and the layers' optical properties, and devise a *set of three principles* to map between them (Secs. 3.2–3.4 and Fig. 5). Based on these principles, we design a calibration target (Sec. 3.5) that can be 3D printed, photographed (or optionally measured with a spectrometer), and then the reflectances of the individual patches are used to fit α and σ_t of each resin (diagram in Fig. 1).

3.1 Reflectance of planar 3D-printed layers

Simulating light transport with subsurface scattering typically requires Monte Carlo volumetric path tracing to solve the *radiative transfer equation (RTE)*. We use Monte Carlo to render 3D printouts in our figures. However, using it *inversely* to calibrate the optical properties is difficult: Monte Carlo with dense scattering and refractive layers is extremely slow to converge and suffers from noise. Despite recent improvements such as recursive control variates [Nicolet et al. 2023] or differential ratio tracking [Nimier-David et al. 2022], we decided to use a computationally much faster approach based on *adding-doubling*. First, we make the following assumptions about the calibration geometry (follow Fig. 3):

- The geometry is plane-parallel.
- The incoming light is directional, covering the entire patch (i.e., the light source is far away or collimated).
- The reflectance is measured orthogonally (at 0°).
- Each patch of the calibration target is sufficiently big, so it can be approximated as infinite in the horizontal plane.
- There is no azimuthal dependency (light interactions are symmetric within a cone shape with a given polar angle).

This geometry significantly simplifies the light transport into a one-dimensional regime. Following previous literature on layered light transport [e.g., Chandrasekhar 1960; Grant and Hunt 1969; Hill et al. 2015; Zeltner and Jakob 2018] and using its nomenclature, we notice that the radiance $L_o(\mu)$ leaving the sample in the direction $\mu = \cos\theta$ can be written as:

$$L_o(\mu) = \int_{-1}^{1} f(\mu, \mu')\, L_i(\mu')\, |\mu'|\, \mathrm{d}\mu', \tag{1}$$

where $L_i(\mu')$ is the incident radiance from $\mu' = \cos\theta'$, and $f(\mu, \mu')$ is the energy transport within the sample between incoming μ' and outgoing μ, where $\mu > 0$ are directions above the sample (upper boundary) and $\mu < 0$ below (lower boundary). The one-dimensional integral can be solved by a *numerical quadrature* using N discrete angles $\mu_1, \dots, \mu_N \in [-1, 1] \setminus \{0\}$ with N weights $w_1, \dots, w_N$:

$$\forall\, k \in \{1, \dots, N\}: \quad L_o(\mu_k) = \sum_{j=1}^{N} f(\mu_k, \mu_j)\, w_j\, |\mu_j|\, L_i(\mu_j). \tag{2}$$

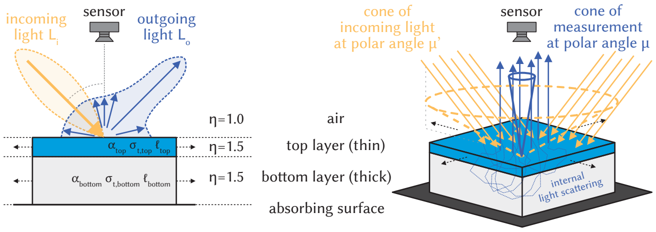

Fig. 3. Our calibration geometry is based on plane-parallel, 1D light transport in a stack of two semi-infinite layers of resins with homogeneous optical properties α, σ_t, η, and thicknesses ℓ (see Table 1). The illumination (as a cone of light) is reflected from the dielectric surface or refracted into the layers. Inside, multiple scattering occurs, after which the photons reach the sensor that is orthogonally placed to avoid the direct mirror reflection.

This set of N equations can be written in a matrix form with an $\mathbb{R}^{N\times N}$ matrix and vectors $\mathbf{L_o}, \mathbf{L_i} \in \mathbb{R}^N$, where the matrix can be split into four submatrices $\mathbf{T_1}, \mathbf{R_1}, \mathbf{R_2}, \mathbf{T_2} \in \mathbb{R}^{N/2\times N/2}$ based on their quadrant, refering to light transport in all directions at each layer, which we visualize in Fig. 4. We can then write:

$$\begin{aligned} \mathbf{L_o} &= \left(\begin{array}{c|c} \mathbf{T_1} & \mathbf{R_1} \\ \hline \mathbf{R_2} & \mathbf{T_2} \end{array}\right) \cdot \mathbf{L_i} = \left(\begin{array}{c|c} \mu{>}0 \;\; \mu'{<}0 & \mu{>}0 \;\; \mu'{>}0 \\ \hline \mu{<}0 \;\; \mu'{<}0 & \mu{<}0 \;\; \mu'{>}0 \end{array}\right) \cdot \mathbf{L_i} \\ &= \left(\begin{array}{c|c} \uparrow \text{upward transmittance} & \searrow\nearrow \text{top reflectance} \\ \hline \nearrow\searrow \text{bottom reflectance} & \downarrow \text{downward transmittance} \end{array}\right) \cdot \mathbf{L_i}. \end{aligned} \tag{3}$$

We use this representation because the submatrices $\mathbf{T_1}, \mathbf{R_1}, \mathbf{R_2}, \mathbf{T_2}$ can be easily computed using *adding-doubling equations* [described in detail in prior works, e.g., Prahl 1995]. For example, for a single homogeneous layer with known α, σ_t, ℓ, we can compute its submatrices with an initialization method followed by *doubling equations*. We can also stack two layers using *adding equations*, which compute the submatrices of the layer stack from the submatrices of the two layers. To work with refractive boundaries, we compute the matrices using the Fresnel equations and we adjust the quadrature points (angles) to account for the refraction, taking into account that certain angles become invalid (Fig. 4, right).

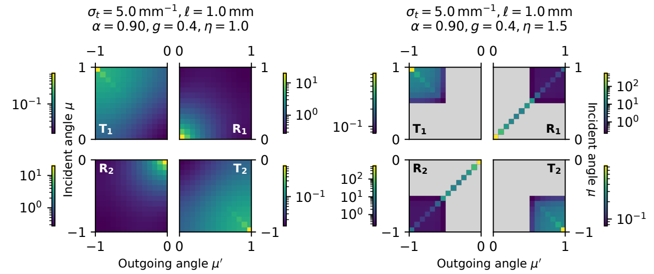

Fig. 4. Examples of the $\mathbf{T_1}, \mathbf{R_1}, \mathbf{R_2}, \mathbf{T_2}$ submatrices used in adding-doubling, visualized as logarithmic intensities of the elements ($14^2 = 196$ elements per submatrix). The spacing between angles is not uniform and is given by the numerical quadrature. The reflection is stronger at grazing angles ($\mu = \mu' \to 0$) due to Fresnel equations and forward scattering. The transmittance is stronger when passing straight through ($\mu = -\mu'$). Note that the angles are from the point of view of the sample, so for the refractive index of $\eta = 1.5$ (right), most of the elements are invalid (gray) as such angles cannot be achieved due to total internal reflection at the refractive boundary.

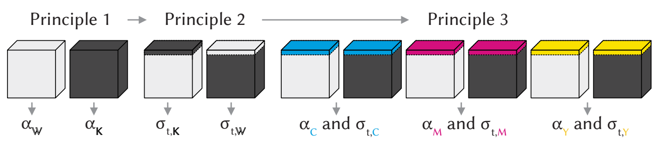

Fig. 5. Our calibration is bootstrapped in three consecutive steps. Principle 1 estimates the albedo α of white and black resins independently, from a single thick layer. With known α, Principle 2 then estimates their extinction coefficients σ_t, from their thin layers printed on top of the opposite color. With known α and σ_t, Principle 3 then estimates the α and σ_t of any remaining resins, from thin layers printed on top of white and black.

In our method, per Fig. 3, we are interested in light being reflected at $\mu = \cos 0^\circ = 1$ (sensor direction) and $\mu' \approx \cos 45^\circ$ (light direction). In practice, we compute all the submatrices for a given stack of resin layers, and then extract the *directional reflectance* $\varrho = L_o(\mu)/L_i(\mu')$ from the corresponding region of the $\mathbf{R_1}$ submatrix. On a modern CPU, with $14^2 = 196$ elements in each submatrix, the equations can be evaluated in only a few milliseconds, and their numerically stable implementations are available as C++ and Python libraries (Sec. 4).

3.2 Principle 1: Estimating α when $\tau \to \infty$

We first consider a single-layer sample with virtually infinite thickness (Fig. 5, left). Intuitively, the thicker the layer is, the less the background influences the reflectance. For example, a thin layer of spilled milk is see-through, but a glass of milk is opaque.

In Fig. 6 (left), we study how the reflectance $\varrho(\alpha, \tau)$ relates to α and τ. We observe that as $\tau \to \infty$, the directional reflectance in our measurement configuration eventually converges. More importantly, the converged reflectance $\varrho(\alpha, \tau)_{\tau\to\infty}$ is strictly related to the material's albedo α and does not depend on its extinction coefficient σ_t. A similar observation was made by Elek et al. [2017, Sec. 6.1, Eq. 4], who found an analytic mapping for a diffusely lit measurement geometry. Notice as α is defined as a ratio, it is highly non-linear and differentiating between, i.e., $\alpha = 0.99$ and 0.999, becomes imporant in practice.

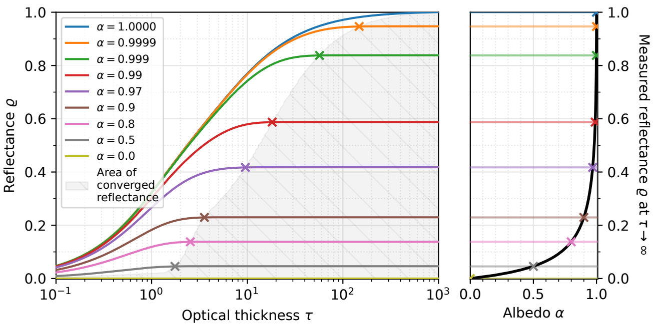

Fig. 6. Principle 1. **Left:** As the optical thickness τ increases, reflectance ϱ converges (the curves flatten, visualized by the × markers and a gray area). It is non-linear and occurs at higher τ for materials with higher albedo α. **Right:** By following the left graph, we construct a one-to-one mapping between the material albedo α and reflectance ϱ.

Having confirmed our intuition, we construct a one-to-one mapping (Fig. 6, right) based on the converged values $\varrho(\alpha, \tau)_{\tau\to\infty}$. For solving the inverse problem, i.e., finding α from a measured directional reflectance $\varrho^\star$, we formulate a one-dimensional optimization:

$$\arg\min_{\alpha} \left| \varrho(\alpha, \tau)_{\tau\to\infty} - \varrho^\star \right|, \tag{4}$$

which has a unique minimum, as the function $\varrho(\alpha, \tau)_{\tau\to\infty}$ is absolutely monotonic.

Discussion. Regarding practicality, this calibration principle is best suited for resins with high extinction σ_t or low albedo α. Otherwise, for high α, the reflectance only converges at high τ (Fig. 6, note the horizontal axis is logarithmic). And, as the relation $\tau = \ell \cdot \sigma_t$ (Table 1) shows, for low extinction σ_t, one would *also* need a thicker layer (ℓ) to compensate for it. Fortunately, white and black resins on which we apply this principle fall into favorable categories. Any white resin must have both high σ_t and high α to be reflective and appear white. Conversely, any black resin must have low α such that it absorbs light and appears black.

3.3 Principle 2: Estimating σ_t with known α

From Principle 1, we can estimate the albedo α of white and black resins. In Principle 2, we want to estimate their extinction σ_t. Although it is irrelevant what color they actually have, it is practical to assume two resins that have at least some contrast. Later in Sec. 5, we show that the contrast does not have to be strong and the method works even for two similar resins (such as light gray and dark gray instead of white and black).

We now construct a scenario where a thin resin layer of α_{top} is printed on top of a thick layer with contrasting albedo $\alpha_{\text{bottom}} \not\approx \alpha_{\text{top}}$ (Fig. 5, middle left). From Principle 1, we know the bottom layer's reflectance is independent of its extinction $\sigma_{t,\text{bottom}}$ or optical thickness τ_{bottom}. The reflectance of the stack thus only depends on $\alpha_{\text{bottom}}, \alpha_{\text{top}}, \tau_{\text{top}}$, denoted as $\varrho(\alpha_{\text{bottom}}, \alpha_{\text{top}}, \tau_{\text{top}})$. In Fig. 7 a subset of the three-dimensional function is plotted. Already, it is evident that the more α_{top} differs from α_{bottom}, the easier it is to discriminate

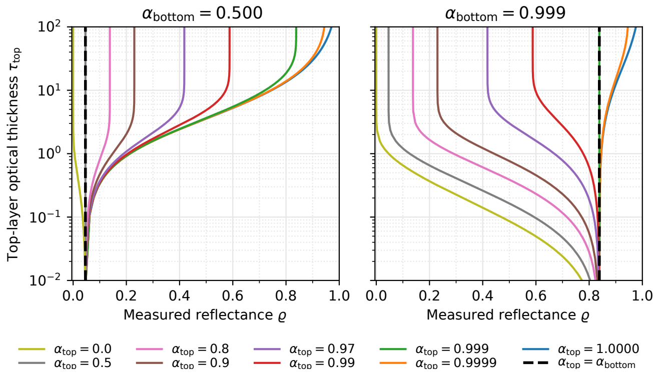

Fig. 7. Principle 2. A thin layer (known α_{top}, unknown τ_{top}) is printed on top of a thick layer (known α_{bottom}, assuming $\tau_{\text{bottom}} \to \infty$, Principle 1). By measuring reflectance ϱ of the layer sandwich, we estimate the optical thickness τ_{top}. Notice that a higher difference between α_{top} and α_{bottom} leads to a bigger range, allowing for higher accuracy.

the top layer τ_{top} (vertical axis) given the measured reflectance $\varrho^{\star}$ (horizontal axis). With both α_{top} and α_{bottom} known from Principle 1, estimating τ_{top} is again a one-dimensional optimization problem:

$$\underset{\tau_{\text{top}}}{\arg\min} \left| \varrho(\alpha_{\text{bottom}}, \alpha_{\text{top}}, \tau_{\text{top}}) - \varrho^{\star} \right|, \tag{5}$$

from which we can compute $\sigma_{\text{t,top}} = \tau_{\text{top}} / \ell_{\text{top}}$ (see Table 1) given that we know how thick the 3D printer printed the top layer (ℓ_{top}).

Discussion. The optimization problem in Eq. 5 has a unique minimum as the function $\varrho(\alpha_{\text{bottom}}, \alpha_{\text{top}}, \tau_{\text{top}})$ in Fig. 7 is monotonic but with two plateaus at either end. Especially if α_{top} is close to α_{bottom}, the absolutely monotonic interval, in other words the well-discriminating range, shrinks. This effectively means a higher likelihood of landing in the upper plateau, which only represents the lower bound of τ_{top}. In practice, this is solvable in two ways: first, by printing the top layer as thin as possible, reducing the value of τ_{top}. And second, as we show later in Sec. 3.5, printing a mixture of the resins, which blends the optical properties and increases robustness.

3.4 Principle 3: Estimating top-layer α, σ_{t}

In Principles 1–2, we found the albedo α and extinction σ_{t} of white and black resins, or generally two resins with different values of α. Having established that, we can calibrate any remaining resins by printing *two samples* for each: a thin layer on top of white, and on top of black (Fig. 5, right). This creates a contrasting scenario in which we observe the translucent resin against two different backings. Iser et al. [2022] already showed that placing a sample against two backgrounds, black and white, allows estimating its optical properties. However, they required a lookup table, precomputed with Monte Carlo, which we avoid by working with fast adding-doubling.

Akin to Principle 2, the reflectance $\varrho(\alpha_{\text{bottom}}, \alpha_{\text{top}}, \tau_{\text{top}})$ (Fig. 7) is measured, but in two variants ϱ_1, ϱ_2 differing by $\alpha_{\text{bottom,1}}, \alpha_{\text{bottom,2}}$. We visualize slices of this four-dimensional parametrization in Fig. 8 and observe plots resembling Iser et al. [2022, Fig. 2a], providing a mapping between $(\alpha_{\text{top}}, \tau_{\text{top}}) \leftrightarrow (\varrho_1, \varrho_2)$. Finding the unknown $(\alpha_{\text{top}}, \tau_{\text{top}})$ is then a two-dimensional optimization problem:

$$\underset{\alpha_{\text{top}}, \tau_{\text{top}}}{\arg\min} \left| \varrho(\alpha_{\text{bottom,1}}, \alpha_{\text{top}}, \tau_{\text{top}}) - \varrho_1^{\star} \right| + \left| \varrho(\alpha_{\text{bottom,2}}, \alpha_{\text{top}}, \tau_{\text{top}}) - \varrho_2^{\star} \right|, \tag{6}$$

where $\varrho_1^{\star}, \varrho_2^{\star}$ are the two reflectance observations, and the extinction coefficient, again, follows $\sigma_{\text{t,top}} = \tau_{\text{top}} / \ell_{\text{top}}$.

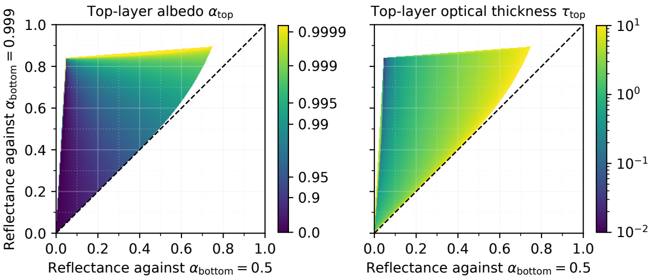

Fig. 8. Principle 3. The same thin layer (unknown α_{top}, $\sigma_{\text{t,top}}$) is printed twice and its reflectance is measured. Once on top of a dark, thick layer (here $\alpha_{\text{bottom}} = 0.5$, horizontal axis). Once on top of a bright, thick layer (here $\alpha_{\text{bottom}} = 0.999$, vertical axis). Two structured mappings are constructed between these reflectances and α_{top} (left), and τ_{top} (right), from which the top-layer resin's properties are estimated.

Discussion. The optimization in Eq. 6 has a unique minimum under most circumstances, as the values visualized in Fig. 6 are monotonic. However, we observe the same limitations as Iser et al. [2022]: if τ_{top} is very low, it becomes impossible to distinguish between different values of albedo α_{top}; conversely, if τ_{top} is very high, the top layer absorbs so much light that we can only estimate the lower bound of τ_{top}. Similarly to Principle 2, we ensure the robustness of the optimization by also printing a mixture diluted with the white resin (Sec. 3.5).

3.5 Designing the calibration target

Capturing the input reflectances for Principles 1–3, we need to 3D print the resin stacks as in Fig. 5. With practicality in mind, we design the calibration target as a single slab (see Fig. 10, top left) of at least 5 mm thickness, split into two areas: one made of white resin, the other of black resin. Thin squares of all resins to be calibrated are placed on top of both areas, including the black and white themselves. In our experiment, the squares were 10 × 10 mm large and 0.675 mm thick. Principle 1 uses the white squares on white resin, and black on black resin, essentially homogeneous blocks. Principle 2 uses the white squares on black, and black on white. And Principle 3 uses the remaining squares.

Additional mixtures. For an ablation study (Sec. 6.1), we also tested larger calibration targets (Fig. 10) containing additional dithered mixtures. In Target B, we added a 10:90 and 90:10 mixture of black and white, and 10:90 mixtures of colors and white. In Target C, we further added 5:95, 10:90, 25:75, and 50:50 ratios, with the intention to increase the robustness of Principles 2 and 3. As absorption and scattering are linear quantities, a mixture of two resins in the proportions $\gamma \in [0, 1]$ for the first and $(1 - \gamma)$ for the second, has:

$$\sigma_{\text{a}} = \gamma \sigma_{\text{a1}} + (1 - \gamma) \sigma_{\text{a2}}, \quad \sigma_{\text{s}} = \gamma \sigma_{\text{s1}} + (1 - \gamma) \sigma_{\text{s2}}, \tag{7}$$

where σ_{a1}, σ_{a2}, σ_{s1}, and σ_{s2} are the absorption and scattering coefficients of the two resins in the mixture, and the conversion equations between σ_{a}, σ_{s}, σ_{t}, and α can be found in Table 1.

4 Implementation

Printing the calibration target. The 3D printer expects instructions where to print each resin within a discrete 3D grid. We wrote a Python script that outputs layer-by-layer bitmaps, encoding where each resin should be printed. The bottom layers are horizontally split into 100% white and 100% black pixels. The top layers are a regular grid of squares with resin mixtures per Sec. 3.5.

As our 3D printer cannot print a linear mixture of two resins, we use dithering. At each pixel within a mixture, we randomly choose the resin given the mixture ratio. The resin droplets are microscopic and the entire layer is large in comparison, so we compute the layer properties with Eq. 7.

The printheads may suffer from clogged nozzles causing imperfections and artifacts such as tiny stripes on the top surface. If that occurs, the top of the sample can optionally be polished. If the 3D printer is equipped with a transparent resin, it is beneficial to print a transparent layer on top of the target to protect the color layers from abrasion. As the color squares in our target are relatively large, minor artifacts are averaged out over the entire patch, and we noticed that small scratches *do not* degrade the calibration quality. Printing in *gloss* mode, which alters the curing intensity of the top layers and prevents coverage with support material, might be beneficial for avoiding user interaction with in-situ calibrations inside the 3D printer.

Capture. The calibration target is placed on a dark, opaque sheet to prevent light transmission from the back of it. We illuminate the front of the target at approximately 45° with roughly collimated light, which can be achieved using a distant light source (more affordable) or a collimating lens. The sensor is placed orthogonally to the sample to avoid specular reflections. To measure RGB optical properties, we used a DSLR camera (Canon EOS E8, RF 100mm $f/2.8$ L Macro lens) positioned at a distance to capture the reflections orthogonally. We placed a small X-Rite color checker in the photographs to allow color corrections of the photos. The photograph was processed semi-automatically with the user selecting the edges of the calibration target, and our Python script would then isolate the individual squares, taking their average reflectance value. We also tested our approach on spectral optical properties with a calibrated spectrometer (Broadcom Qwave VIS, 350–880 nm, 0.5 nm resolution) pointed at each target square, one by one. To normalize the spectral measurements, we captured a Spectralon with 99% diffuse reflectance.

Fitting and performance. The fitting requires the computation of layer reflectances via Eq. 3. We wrote a Python script computing the adding-doubling equations based on the `iadpython` package [Prahl 2018], which ensures numerical stability and includes the refractive boundaries. Our plots in Figs. 6–8 were also based on these equations. Fitting the optical properties of the individual resins was done following our Principles 1–3 (Secs. 3.2–3.4). For the derivative-free optimizations of the one-dimensional and two-dimensional functions, we used an adaptive sampling strategy implemented in the `adaptive` Python package [Nijholt et al. 2019]. The optimization is fast and scales with the number of observations and channels (wavelengths) to fit. For Target B, the optimization took about 2 minutes in RGB and around 8.5 minutes spectrally with a 25 nm resolution, on a modern desktop CPU (Intel Core i9-13900K). As the fitting is executed in Python, we believe that further speed optimizations could be performed.

Preview rendering. For the photorealistic renders of 3D printouts in this paper, we employed Monte Carlo volumetric path tracing in scenes with manually aligned cameras and lights. The objects are represented by a heterogeneous grid, where each voxel corresponds to one resin with the calibrated α, σ_t, and $g = 0.4$. The surfaces are assumed to be dielectric with $\eta = 1.5$. The slabs were rendered as smooth dielectrics, the figurine was rendered with surface roughness 0.2 and the eye model with 0.05 as it had a smoother surface, where the roughness was modeled with the Trowbridge–Reitz (GGX) distribution [Trowbridge and Reitz 1975; Walter et al. 2007]. The rendering used Mitsuba 3 [Jakob et al. 2022], which supports both RGB and spectral rendering with an arbitrary spectral resolution.

5 Synthetic evaluation

Before evaluating our calibration on real resins (Sec. 6), we perform a synthetic stress test on virtual simulations. The goal of the experiment is to stress test whether our calibration supports a wide range of optical properties. As our method requires at least one reflective ("white") and one absorptive ("black") resin, we also test what happens if both of these resins are optically similar to each other, i.e., they are not really white and black but rather light gray and dark gray. We also compare that to the measurement method of Iser et al. [2022]. All experiments in this section are run virtually by simulating the inputs (reflectances) to the methods with added random noise (normal distribution with $\sigma = 0.005$, which corresponds to 0.5% of the reflectance of a white diffuse surface). All results of this section are visible in Fig. 9.

Stress test 1. For our first test, we set the optical properties of the "white" and "black" resins to sufficiently different constant values: $\alpha = 0.999$, $\sigma_t = 20\,\text{mm}^{-1}$ for the white resin and $\alpha = 0.5$, $\sigma_t = 5\,\text{mm}^{-1}$ for the black. For the "colors", we artifically construct four resins whose extinction coefficient σ_t continuously varies from 0.1 to 30.0 mm^{-1} and their albedo $\alpha \in \{0.1, 0.9, 0.99, 0.999\}$. We believe that this selection sweeps through the reasonable ranges that one can expect in real conditions (see further Sec. 6).

Stress test 2. In our second test, we attempt to break our calibration method by using "white" and "black" resins that are optically similar to each other. We use the same "color" resins as in the first test, but we set the "white" to $\alpha = 0.99$, $\sigma_t = 5\,\text{mm}^{-1}$ (light gray) and the "black" to $\alpha = 0.90$, $\sigma_t = 5\,\text{mm}^{-1}$ (dark gray).

Results using Iser et al. [2022]. In the older calibration method, each resin is measured independently and there is no requirement for a white and black resin. Hence, between the two stress tests, the four "colors" are estimated almost identically and the small differences are caused by the random additive noise. We use the exact same pre-computed lookup tables (for $g = 0.4$) and thicknesses as in the original publication. The calibration is based on two samples for each resin: 0.38 and 0.79 mm thin, polished, and homogeneous slabs. Practically, it is very difficult to achieve samples thinner than that. As we can see in Fig. 9, the accuracy of the calibration is limited by the minimum thickness, which makes it impossible to measure high extinction σ_t with low albedo α and likewise high α with low σ_t.

Our results. In the first stress test using calibration Targets B and C, our calibration successfully handles the entire range of $\sigma_t \in [0.1, 30.0]\text{mm}^{-1}$ and $\alpha \in \{0.1, 0.9, 0.99, 0.999\}$. We observe that Target A is insufficient for high σ_t with low α and the additional samples in Target B are required. In the second stress test, we can see that our method is very robust and accurate even in the difficult case of using gray resins in the bottom layers. The only difficult range for the calibration is high α with low σ_t.

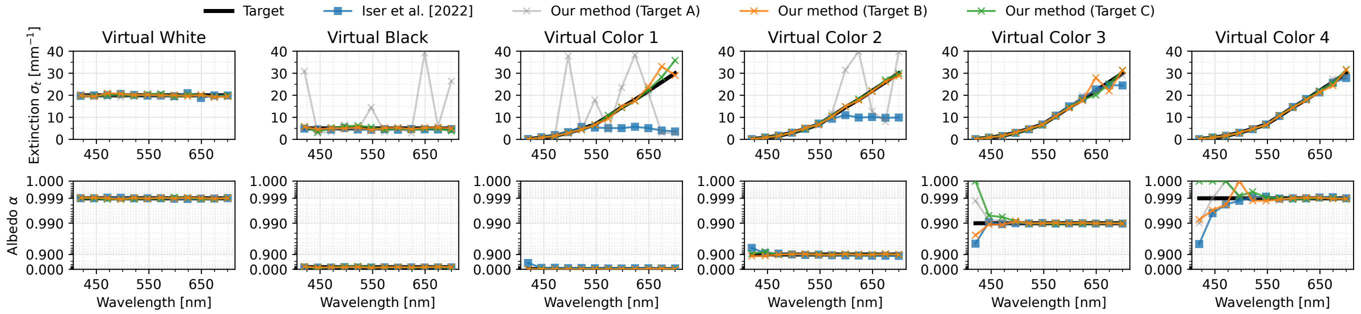

(a) Stress test 1: Scenario with a wide range of optical properties that real resins likely have

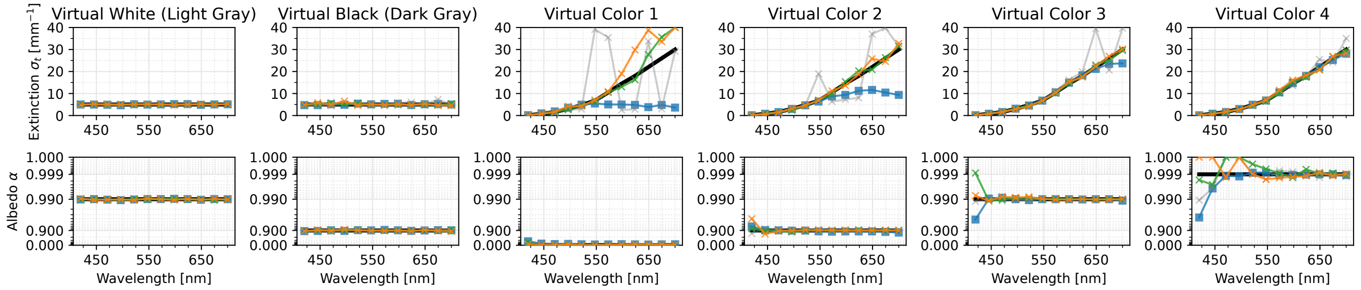

(b) Stress test 2: Scenario in which the "white" and "black" resins are similar to each other, which is more difficult for our method

Fig. 9. Synthetic evaluation of the optical calibration on two sets of six virtual resins ("white", "black", and four "colors"). While Iser et al. [2022] (blue) has low accuracy for resins with high extinction σ_t and low albedo α, our method recovers the wide range of optical properties significantly better. It also illustrates that our larger calibration Targets B and C provide more stable results than Target A. More information on the experiment: text in Sec. 5.

6 Real calibration results

We evaluated our method in real-life conditions on several different sets of samples to examine how well it generalizes to various colors and geometric shapes. All samples were printed on a Stratasys J750 PolyJet 3D printer with a horizontal resolution of 300 × 600 DPI and vertical resolution of ≈ 940 DPI (27 µm layer height). The calibration targets were gently polished, the remaining samples were not and only their support material was cleaned. The printer was equipped with the following resins: VeroVivid (cyan, magenta, yellow), BlackPlus, PureWhite, and VeroClear. All result photos were captured in a dark room, with the printouts illuminated by LED lights. The images were published as raw as possible, with color corrections based on X-Rite ColorCheckers.

In some of our experiments, we provide direct comparisons to the calibration results of Iser et al. [2022]. We followed their calibration procedure and show results fitted to $g = 0.4$, same as they did in their Sec. 5. These comparisons are valuable, as they are the only affordable previous work that handles multiple scattering and spectral rendering. Their results exhibit difficulties to fit resins with high σ_t, mainly the white and yellow resins at wavelengths between 400 nm to 500 nm. Such measurements would require almost impossibly thin samples that can only be polished on expensive, specialized machines. In the results that we show, it is noticable in yellow hues, which are not as saturated as they should be. In contrast, our method succeeded in fitting these properties without any problems.

Printable files from this section are attached in the supplement.

6.1 Color and spectral accuracy on resin mixtures

Our first experiment verifies the color accuracy for halftoned resin mixing. We printed 121 resin mixtures, 0.675 mm thick, once on top of white and once on the black resin, with 242 total combinations (Fig. 11). This allows observing the translucency and how the color depends on the layers below. Resins with low α appear dark on top of a dark layer, even though they can appear bright on white.

In Fig. 10, we show a *quantitative evaluation* on these 242 patches with different calibrations based on Targets A–C. We observe that *spectral calibrations* outperform RGB, and that 25 nm spectral bins are sufficient, with no requirement for a finer spectral resolution. We also confirmed that a larger calibration Target B provides an advantage over the smaller Target A, mainly because our resins are highly absorptive, which is difficult to measure from 100% concentrations. We observe that our method significantly outperforms Iser et al. [2022], who struggled with highly absorptive resins. Finally, an even larger Target C does not seem to provide any advantage. Still, we used the spectral calibration (`Target C, 5nm`) to compute the rest of our results, unless otherwise noted. In Fig. 11, we also show the color prediction for each of the 242 patches, and then the spectral curves for a selection of 16 patches. The spectral predictions are computed using adding-doubling, illuminated by the same LED spectrum as the measurements, and converted to sRGB using the CIE XYZ 2° color matching functions. We observe a high color accuracy that is consistent across all color mixtures with a mean CIE DeltaE 2000 of below 2.

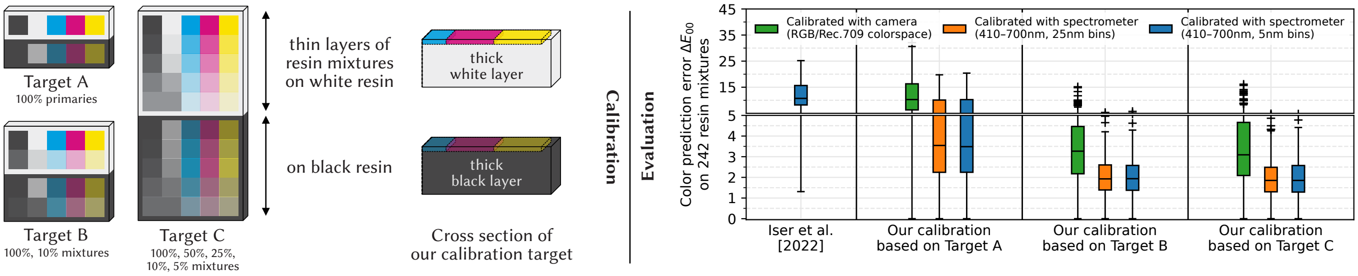

Fig. 10. **Left:** Three variants of our calibration target with 10, 20 and 50 patches. The primaries and mixtures are printed in a thin layer on top of white and black blocks. **Right:** A quantitative comparison against Iser et al. [2022] on CIE DeltaE 2000 (↓) over additional mixtures (Fig. 11) using three different capturing devices: a DSLR camera (RGB) and two spectrometers downsampled to 25nm and 5nm resolutions respectively. Even an RGB calibration on our Target B can outperform previous work, while a higher-resolution spectrometer and more mixtures (Target C) bring little benefit.

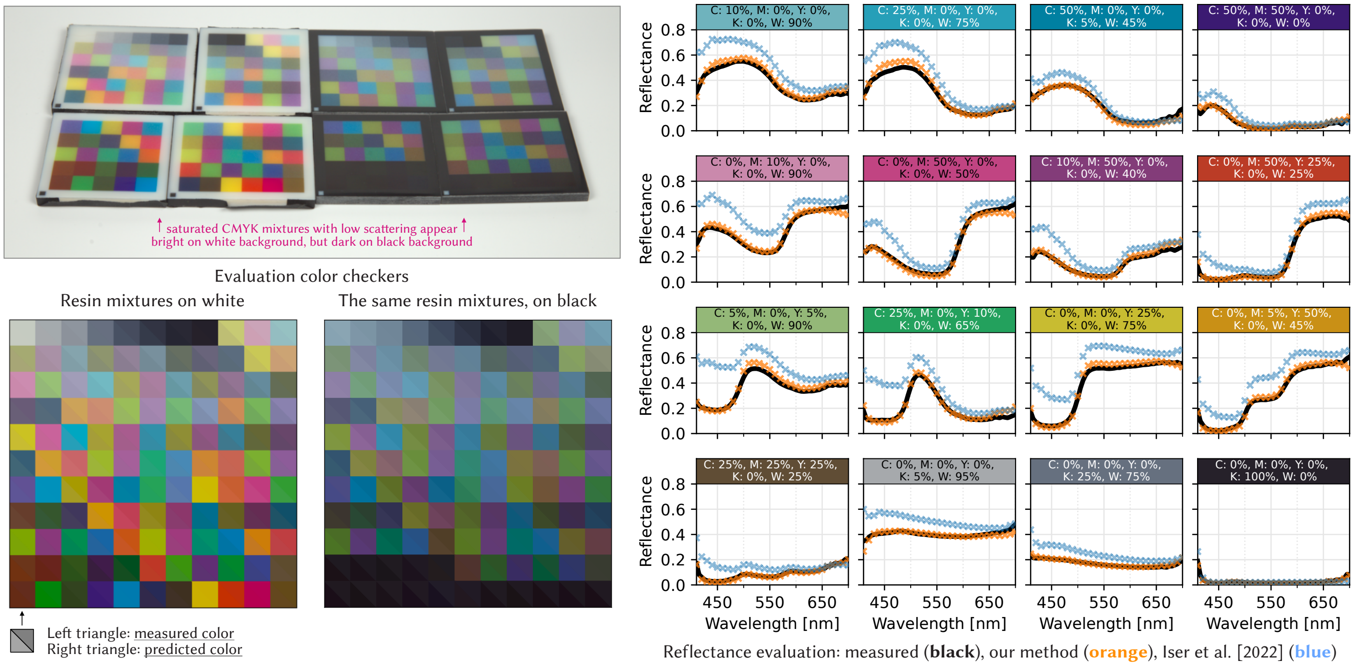

Fig. 11. **Left:** The 3D printed color checkers with 242 patches used for evaluation. The top shows a photograph for visualization, and the bottom shows the spectrally measured colors overlayed with their spectral predictions from adding-doubling using the `(Target C, 5nm)` calibration. **Right:** The spectral reflectance curves for 16 patches comparing measurements and predictions both from our calibration and from Iser et al. [2022].

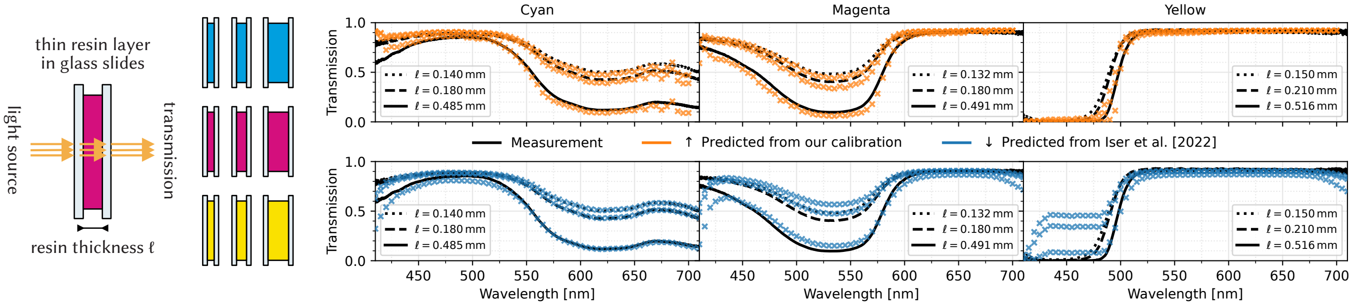

Fig. 12. Evaluation on a set of thin samples from the three colored resins. The transmission spectrum of a collimated beam through three thicknesses is measured and compared to spectral adding-doubling predictions using our `(Target C, 5nm)` calibration and Iser et al. [2022].

6.2 Spectral transmission on thin resin samples

Showing further generalization of our calibrations to various layer thicknesses ℓ, we compare to the type of calibration targets that Iser et al. [2022] are using. We therefore manually prepared 9 samples of thin resin layers enclosed in an index-matched glass sandwich. In Fig. 12, we show spectral measurements and predictions of the collimated transmission through these samples obtained by adding-doubling on the `(Target C, 5nm)` calibration. We observe that our results are similar to Iser et al. [2022], except for the highly-absorbing yellow resin, where our results are better.

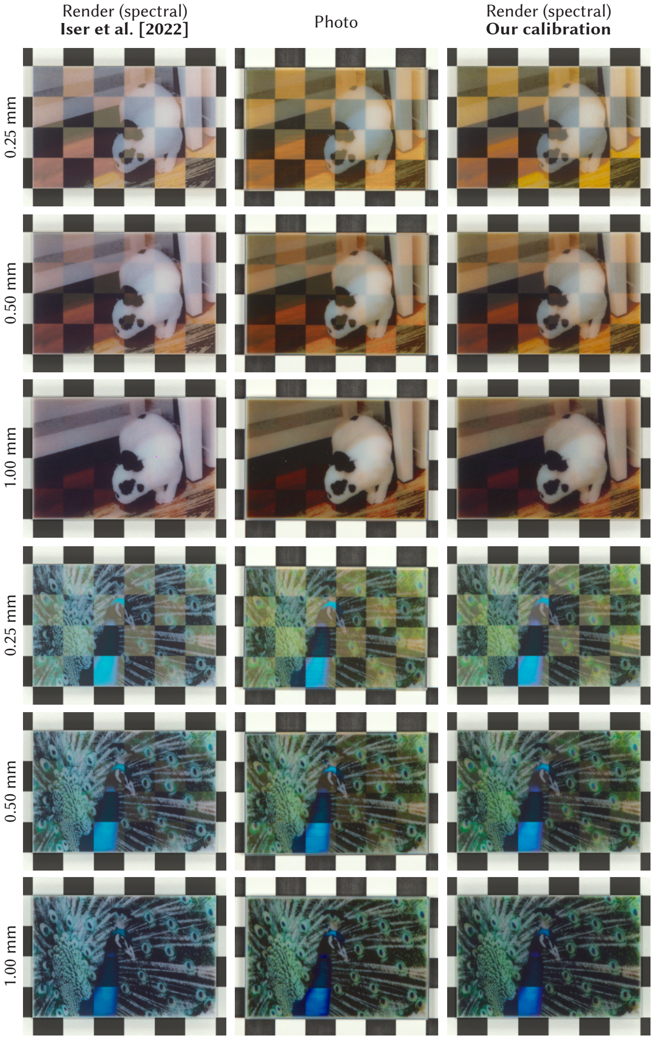

Fig. 13. Comparing photographs of thin, translucent textures to Monte Carlo renderings. Two textures (*Loris bunny* and *peacock*) are each printed three times: 0.25, 0.50, and 1.00 mm thin, enclosed in additional 0.50 mm clear resin. A checkerboard pattern printed with a laser printer on smooth paper is placed below. Our calibration leads to precise simulations of the translucency and colors. While Iser et al. [2022] can also predict the translucency, they have a “milky appearance" and cannot achieve deep yellows.

6.3 Color accuracy on thin translucent textures

Following the previous experiment on thin, homogeneous samples, we also prepared thin, textured samples. We printed 45 × 30 mm large and 0.25–1.00 mm thin textures (halftoned photographs) that were enclosed in an additional 0.5 mm clear resin on top and bottom. As the texture itself is very thin, the background below the slab is partially visible. Because our calibration accounts for both absorption and scattering, we are capable of accurately simulating the translucency. In Fig. 13, we demonstrate a direct comparison between photos and our renders on a checkerboard backing sheet. The goal of this experiment is to prove that our calibration can be used for highly translucent thin objects and accurately predict how the background can be seen through.

6.4 Color accuracy on textures on thick white slabs

While above we printed thin textures enclosed in clear resin to showcase translucency, a more common scenario is printing textures on thick printouts. In this experiment, we printed thick slabs, each about 55 × 42 mm large and 5.0 mm thick, where approximately 0.5 mm thickness is textured and the remaining 4.5 mm is white resin. Four colorful, public domain paintings were 3D printed using an algorithm inspired by Sumin et al. [2019]. The goal is to render a 3D-printed grid of resins and to achieve a good match with the photographs of the printouts. For this purpose, we algorithmically aligned the two images, optimizing for the 2D translation, rotation, and scaling factors as well as adjusted the exposure of the renders. In Fig. 14, we demonstrate that our spectral Monte Carlo renders based on `(Target C, 5nm)` are highly accurate, with a pixel-based prediction error about 2.5× lower than of Iser et al. [2022]. Please note that a perfect color match cannot be ensured unless the spectral sensitivity curves of the camera and lens are taken into account during renderings. Hence, the ΔE_{00} values in the insets are best interpreted relative to each other, and not in absolute terms.

6.5 Color accuracy on 3D shapes

We also evaluate 3D shapes (Fig. 15), for which we chose two objects: a model of a human eye, which has a simpler geometry but high-resolution texture, and a figurine, with complex geometry such as thin arms and legs. In addition to spectral Monte Carlo renders based on `(Target C, 5nm)`, RGB renderings based on `(Target B, RGB)` calibrations are shown. We observe that there is little practical difference between our RGB and spectral rendering, which is positive as RGB calibrations are faster and more affordable. It seems, again, that Iser et al. [2022] suffer from mismatched yellow hues. Note that side-by-side comparisons on 3D shapes are significantly more difficult than on flat geometries as the object's appearance is influenced by postprocessing (such as removing the residues of support materials), surface treatment, alignment, illumination geometry, shadows, and similar. Therefore, reporting ΔE_{00} values would be meaningless and the comparison is purely subjective.

6.6 Phase function anisotropy coefficient

Our method is not aimed at calibrating the phase function anisotropy coefficient g. Throughout this paper, we assume $g = 0.4$ (justified in

Fig. 14. Comparing photographs of four textured slabs (center) to aligned, spectral Monte Carlo renderings on either side. Our calibration on (`Target C, 5nm`) provides a better color match than Iser et al. [2022] as evident from the mean color error in the center regions of the difference images (first & last column). All textures in this figure are adaptations of old paintings that are in the public domain.

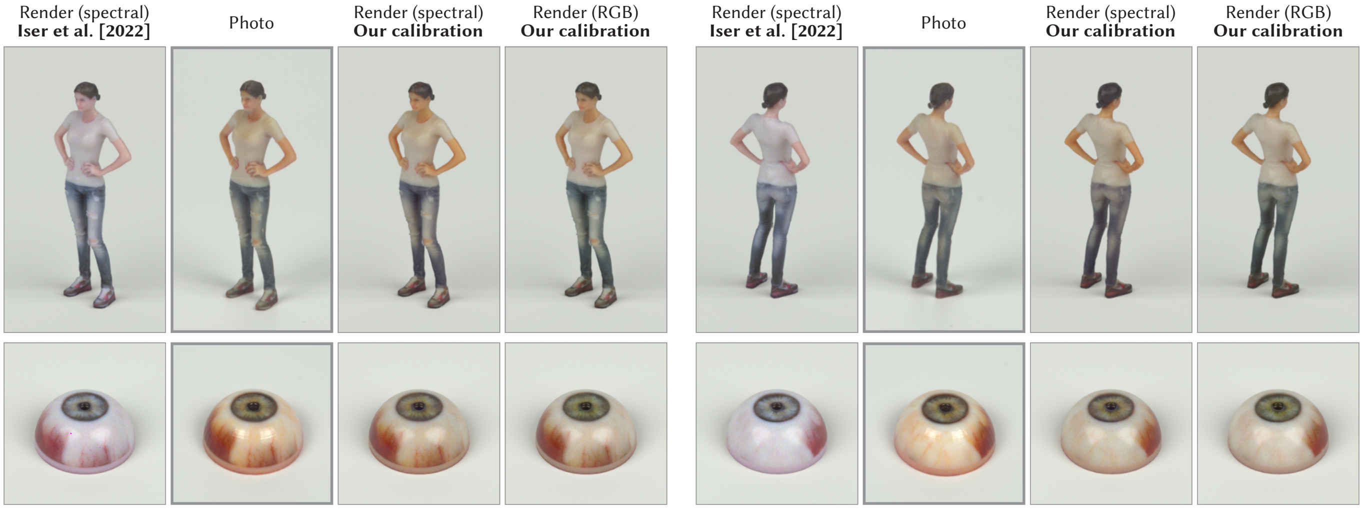

Fig. 15. A qualitative comparison between photographs and Monte Carlo renderings on two 3D objects. The spectral calibrations of Iser et al. [2022] and our (`Target C, 5nm`) calibration differ greatly, especially in the hues containing yellow such as the skin and the veined sclera. The difference to our (`Target B, RGB`) calibration is less noticeable. Figurine by fablabbudapest is licensed under CC BY 4.0. Eye by Alexander Antipov is licensed under CC BY 4.0.

Sec. 2.2). To verify that this choice is not detrimental to color accuracy, we executed the spectral calibration script on Target B with 25 nm bins for a varying $g \in \{-0.95, 0.90, \ldots, 0.00, \ldots, 0.90, 0.95\}$. Each choice of g (fixed during each individual calibration) can converge to different (α, σ_t) for each resin. We then simulated the reflectances of the 242 color patches from Sec. 6.1 and computed the color prediction error for each result (Fig. 16).

We observe that the median error is higher for $g < -0.5$ (stronger backward scattering) and for $g > 0.5$ (stronger forward scattering). We also observe that the error variance and the number of outliers decreases for higher g, which results in more consistent color predictions. In conclusion, it seems that the choice of $g = 0.4$ is valid and does not hinder color accuracy. In fact, there is a wide range of anisotropies g that give similar color accuracy on our reflectance data, so it is not possible to select any g as clearly the best choice. A similar observation was also made in the method of Abu Rmaileh et al. [2025] and it is not surprising: equivalence classes (also called *similarity relations*) in light-scattering materials have been described in the past [Wyman et al. 1989; Zhao et al. 2014].

6.7 Spectral extinction coefficient accuracy

Our final validation experiment is based on comparing our fitted optical properties to accurate measurements performed in an optical lab with an integrating sphere. We compare to the results obtained by Kissel et al. [2025, Fig. 5], who measured their own samples of the resins of the same brand (Stratasys VeroVivid: cyan, magenta, yellow). A full comparison was not possible as we did not have access to the same white and black resins (UltraWhite and UltraBlack). Note that Kissel et al. assumed that cyan, magenta, and yellow were non-scattering, i.e., $\sigma_s = 0$ or equivalently $\alpha = 0$, whereas our calibration method includes scattering for all resins. Simply comparing the σ_a obtained by each method would be wrong: a collimated beam of light traveling through the material loses light energy by both absorption and scattering, so reducing one of them to zero necessarily increases the other estimate. Therefore, we take into account the entire extinction along the light beam and compute a reduced extinction coefficient computed as $\sigma_t' = \sigma_a + \sigma_s' = \sigma_a + \sigma_s \cdot (1 - g)$. In Fig. 17, we can see that our results for the three resins are very close to the results obtained by Kissel et al. [2025]. The only differences can be observed for wavelengths with low extinctions, where even Kissel et al. observed high variance.

7 Conclusion

Full-color 3D printing is challenging because of subsurface scattering. A body of work has improved the printing quality *given* the resin's optical properties. However, finding these properties has been difficult and has relied on expensive laboratory equipment or excessive manual work. In this paper, we present a calibration technique that can readily be performed in the field. The results are directly applicable for the rendering of 3D printouts, to visualize the printouts before they are printed, hence saving material costs by avoiding failed prints, and enabling automatic appearance enhancement using the existing scattering-aware optimization pipelines. We expect the importance of our calibration technique to raise in the near future, as more affordable full-color 3D printers are being developed, and the market is slowly opening to a wider audience.

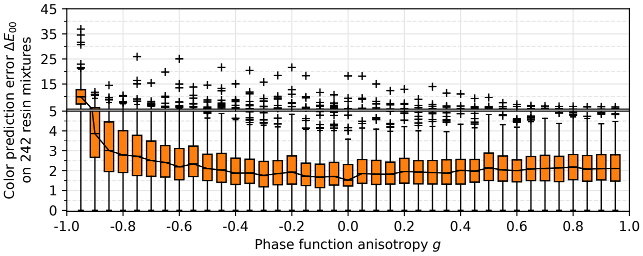

Fig. 16. A quantitative evaluation of the color accuracy when the calibrations are performed with varying phase function anisotropy coefficients. We visualize the CIE DeltaE 2000 color difference metric (↓) between predicted and measured reflectances of 242 resin mixtures.

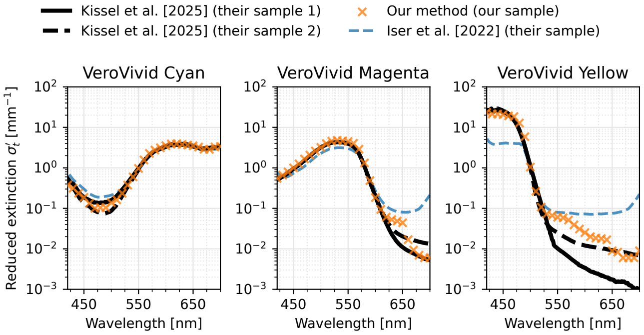

Fig. 17. Reduced extinction coefficients calculated from the measurements of Kissel et al. [2025], Iser et al. [2022], and us. Each measurement was done on a different sample but of the same resin family from the same manufacturer. The data from Kissel et al. were measured using integrating spheres and serve as ground truth.

For the future, we could forsee a complete embedding in the 3D printers. When a new batch of resins is installed, the printer would print our small calibration target, and a built-in RGB or multispectral sensor would measure the reflectances. A calibration algorithm could then, within a couple of minutes, provide the optical properties to the slicing algorithm, without any user intervention.

Limitations. The method assumes that white and black resins are calibrated together with the colors. In theory, one might want to calibrate a resin set that does not contain white and/or black. In that case, there are two possible approaches: first, we showed in Sec. 5 that the method also works for resins with a lower contrast (such as light gray and dark gray instead of white and black); second, certain 3D printers allow printing on top of existing objects, so one could print resins on top of existing white and black surfaces. Another limitation is calibrating a clear resin: when a thin layer of clear is printed, it can be treated as fully transparent, which is what we did in our experiments. However, thick layers of several centimeters of clear resin usually have a yellow color cast. Our method could still be used to calibrate the absorption in such case, but the top layer would need to be sufficiently thick to ensure the absorption could be detected. Finally, our method cannot estimate the refractive index η nor the anisotropy coefficient g. It is reasonable to expect that most resins will be around $\eta \approx 1.5$, which is common for polymers. As for the anisotropy, we showed in Sec. 6.6 that due to similarity relations, it seems that an exact match is not required as the color accuracy on printed mixtures remains similar for a wide range of anisotropies g.

Acknowledgments

We would like to thank Alexandr Lazarov and Kateřina Huráková from Czech Technical University for providing access to a 3D printer and for its maintenance. We thank the authors of the 3D models in Fig. 15 for releasing them under a permissive license. We thank everyone else who supported our work, whether directly or indirectly.

This project has received funding from the European Union's Horizon 2020 research and innovation programme under the Marie Skłodowska-Curie grant agreement No 956585. This work was further supported by the Charles University grant SVV-260822.

References

Lubna Abu Rmaileh and Alan Brunton. 2023. Meso-Facets for Goniochromatic 3D Printing. *ACM Transactions on Graphics* 42, 4 (Aug. 2023), 1–12. doi:10.1145/3592137

Lubna Abu Rmaileh, Philipp Nguyen, Alexander Kissel, and Philipp Urban. 2025. Determining intrinsic optical properties of 3D printing materials. *Optics Express* 33, 13 (June 2025), 28493. doi:10.1364/OE.559881

Vahid Babaei, Kiril Vidimče, Michael Foshey, Alexandre Kaspar, Piotr Didyk, and Wojciech Matusik. 2017. Color Contoning for 3D Printing. *ACM Transactions on Graphics* 36, 4 (July 2017), 1–15. doi:10.1145/3072959.3073605

Christoph Bader, Dominik Kolb, James C. Weaver, Sunanda Sharma, Ahmed Hosny, João Costa, and Neri Oxman. 2018. Making data matter: Voxel printing for the digital fabrication of data across scales and domains. *Science Advances* 4, 5 (May 2018), eaas8652. doi:10.1126/sciadv.aas8652 Publisher: American Association for the Advancement of Science.

Florian Bergmann, Florian Foschum, Ralf Zuber, and Alwin Kienle. 2020. Precise determination of the optical properties of turbid media using an optimized integrating sphere and advanced Monte Carlo simulations. Part 2: experiments. *Applied Optics* 59, 10 (April 2020), 3216. doi:10.1364/AO.385939

Benedikt Bitterli, Srinath Ravichandran, Thomas Müller, Magnus Wrenninge, Jan Novák, Steve Marschner, and Wojciech Jarosz. 2018. A radiative transfer framework for non-exponential media. *ACM Transactions on Graphics* 37, 6 (2018), 225:1–225:17. doi:10.1145/3272127.3275103

Alan Brunton, Can Ates Arikan, Tejas Madan Tanksale, and Philipp Urban. 2018. 3D printing spatially varying color and translucency. *ACM Transactions on Graphics* 37, 4 (Aug. 2018), 1–13. doi:10.1145/3197517.3201349

Alan Brunton, Can Ates Arikan, and Philipp Urban. 2015. Pushing the Limits of 3D Color Printing: Error Diffusion with Translucent Materials. *ACM Trans. Graph.* 35, 1 (Dec. 2015), 4:1–4:13. doi:10.1145/2832905

S. Chandrasekhar. 1960. *Radiative Transfer.* Dover Publications, New York.

Danwu Chen and Philipp Urban. 2021. Deep learning models for optically characterizing 3D printers. *Optics Express* 29, 2 (Jan. 2021), 615–631. doi:10.1364/OE.410796 Publisher: Optica Publishing Group.

Jorge Condor, Michal Piovarci, Bernd Bickel, and Piotr Didyk. 2023. Gloss-Aware Color Correction for 3D Printing. In *ACM SIGGRAPH 2023 Conference Proceedings (SIGGRAPH '23).* Association for Computing Machinery, New York, NY, USA, 1–11. doi:10.1145/3588432.3591546

Eugene D'Eon and Geoffrey Irving. 2011. A quantized-diffusion model for rendering translucent materials. *ACM Transactions on Graphics* 30, 4 (July 2011), 56:1–56:14. doi:10.1145/2010324.1964951

Yue Dong, Jiaping Wang, Fabio Pellacini, Xin Tong, and Baining Guo. 2010. Fabricating spatially-varying subsurface scattering. *ACM Transactions on Graphics* 29, 4 (July 2010), 62:1–62:10. doi:10.1145/1778765.1778799

Oskar Elek, Denis Sumin, Ran Zhang, Tim Weyrich, Karol Myszkowski, Bernd Bickel, Alexander Wilkie, and Jaroslav Křivánek. 2017. Scattering-aware Texture Reproduction for 3D Printing. *ACM Transactions on Graphics* 36, 6 (Nov. 2017), 1–15. doi:10.1145/3130800.3130890

Oskar Elek, Ran Zhang, Denis Sumin, Karol Myszkowski, Bernd Bickel, Alexander Wilkie, Jaroslav Křivánek, and Tim Weyrich. 2021. Robust and practical measurement of volume transport parameters in solid photo-polymer materials for 3D printing. *Optics Express* 29, 5 (March 2021), 7568–7588. doi:10.1364/OE.406095 Publisher: Optical Society of America.

Willemijn Elkhuizen, Tessa Essers, Yu Song, Jo Geraedts, Clemens Weijkamp, Joris Dik, and Sylvia Pont. 2020. Gloss, Color, and Topography Scanning for Reproducing a Painting's Appearance Using 3D Printing. *Journal on Computing and Cultural Heritage* 12, 4 (Jan. 2020), 1–22. doi:10.1145/3317949

Florian Foschum, Florian Bergmann, and Alwin Kienle. 2020. Precise determination of the optical properties of turbid media using an optimized integrating sphere and advanced Monte Carlo simulations. Part 1: theory. *Applied Optics* 59, 10 (April 2020), 3203. doi:10.1364/AO.386011

J. R. Frisvad, S. A. Jensen, J. S. Madsen, A. Correia, L. Yang, S. K. S. Gregersen, Y. Meuret, and P.-E. Hansen. 2020. Survey of Models for Acquiring the Optical Properties of Translucent Materials. *Computer Graphics Forum* 39, 2 (2020), 729–755. doi:10.1111/cgf.14023

Ioannis Gkioulekas, Shuang Zhao, Kavita Bala, Todd Zickler, and Anat Levin. 2013. Inverse volume rendering with material dictionaries. *ACM Transactions on Graphics (TOG)* 32, 6 (2013), 162:1–162:13. doi:10.1145/2508363.2508377 Publisher: ACM New York, NY, USA.

Ian Philip Grant and G. E. Hunt. 1969. Discrete space theory of radiative transfer I. Fundamentals. *Proceedings of the Royal Society of London. A. Mathematical and Physical Sciences* 313, 1513 (Oct. 1969), 183–197. doi:10.1098/rspa.1969.0187

Tanzima Habib, Phil Green, Peter Nussbaum, Phil Green, and Peter Nussbaum. 2023. An Appearance Reproduction Framework for Printed 3D Surfaces. *Journal of Imaging Science and Technology* 67 (Sept. 2023), 1–10. doi:10.2352/J.ImagingSci.Technol.2023.67.5.050413 Publisher: Society for Imaging Science and Technology.

Miloš Hašan, Martin Fuchs, Wojciech Matusik, Hanspeter Pfister, and Szymon Rusinkiewicz. 2010. Physical reproduction of materials with specified subsurface scattering. *ACM Transactions on Graphics* 29, 4 (July 2010), 61:1–61:10. doi:10.1145/1778765.1778798

L. G. Henyey and J. L. Greenstein. 1941. Diffuse radiation in the Galaxy. *Astrophysical Journal* 93 (Jan. 1941), 70–83. doi:10.1086/144246

Stephen Hill, Stephen McAuley, Brent Burley, Danny Chan, Luca Fascione, Michał Iwanicki, Naty Hoffman, Wenzel Jakob, David Neubelt, Angelo Pesce, and Matt Pettineo. 2015. Physically based shading in theory and practice. In *ACM SIGGRAPH 2015 Courses.* ACM, Los Angeles California, 1–8. doi:10.1145/2776880.2787670

Tomáš Iser, Tobias Rittig, Emilie Nogué, Thomas Klaus Nindel, and Alexander Wilkie. 2022. Affordable Spectral Measurements of Translucent Materials. *ACM Transactions on Graphics* 41, 6 (Dec. 2022), 1–13. doi:10.1145/3550454.3555499

Wenzel Jakob, Sébastien Speierer, Nicolas Roussel, Merlin Nimier-David, Delio Vicini, Tizian Zeltner, Baptiste Nicolet, Miguel Crespo, Vincent Leroy, and Ziyi Zhang. 2022. Mitsuba 3 renderer. https://mitsuba-renderer.org.

Adrian Jarabo, Carlos Aliaga, and Diego Gutierrez. 2018. A radiative transfer framework for spatially-correlated materials. *ACM Transactions on Graphics* 37, 4 (Aug. 2018), 1–13. doi:10.1145/3197517.3201282

Wojciech Jarosz. 2008. *Efficient Monte Carlo Methods for Light Transport in Scattering Media.* PhD Thesis. UC San Diego.

Henrik Wann Jensen, Stephen R. Marschner, Marc Levoy, and Pat Hanrahan. 2001. A practical model for subsurface light transport. In *Proceedings of the 28th annual conference on Computer graphics and interactive techniques - SIGGRAPH '01.* ACM Press, 511–518. doi:10.1145/383259.383319

Alwin Kienle, Michael S. Patterson, Nora Dögnitz, Roland Bays, Georges Wagnières, and Hubert van den Bergh. 1998. Noninvasive determination of the optical properties of two-layered turbid media. *Applied Optics* 37, 4 (Feb. 1998), 779–791. doi:10.1364/AO.37.000779 Publisher: Optica Publishing Group.

Alexander Kissel, Philipp Nguyen, David Hevisov, Florian Foschum, and Alwin Kienle. 2025. Optical property-based rendering of 3D prints. *Optics Express* 33, 7 (April 2025), 15187. doi:10.1364/OE.553642

Paul Kubelka and Franz Munk. 1931. Ein Beitrag zur Optik der Farbanstriche. *Zeitschrift für Technische Physik* 12 (1931), 593–601.

Sven Leyre, Youri Meuret, Guy Durinck, Johan Hofkens, Geert Deconinck, and Peter Hanselaer. 2014. Estimation of the effective phase function of bulk diffusing materials with the inverse adding-doubling method. *Applied Optics* 53, 10 (April 2014), 2117. doi:10.1364/AO.53.002117

Emiliano Luci, Fabio Pellacini, and Vahid Babaei. 2024. Differentiable Modeling of Material Spreading in Inkjet Printing for Appearance Prediction. In *SIGGRAPH Asia 2024 Conference Papers.* ACM, Tokyo Japan, 1–10. doi:10.1145/3680528.3687598

Yuki Minetomo, Hiroyuki Kubo, Takuya Funatomi, Mikio Shinya, and Yasuhiro Mukaigawa. 2018. Acquiring non-parametric scattering phase function from a single image. *Computational Visual Media* 4, 4 (Dec. 2018), 323–331. doi:10.1007/s41095-018-0122-z

Kazuki Nagasawa, Shoji Yamamoto, Wataru Arai, Kunio Hakkaku, Chawan Koopipat, Keita Hirai, and Norimichi Tsumura. 2022. Fabrication of a Human Skin Mockup with a Multilayered Concentration Map of Pigment Components Using a UV Printer. *Journal of Imaging* 8, 3 (March 2022), 73. doi:10.3390/jimaging8030073 Number: 3 Publisher: Multidisciplinary Digital Publishing Institute.

Kazuki Nagasawa, Junki Yoshii, Shoji Yamamoto, Wataru Arai, Satoshi Kaneko, Keita Hirai, and Norimichi Tsumura. 2021. Prediction of the layered ink layout for 3D printers considering a desired skin color and line spread function. *Optical Review*

28, 4 (July 2021), 449–461. doi:10.1007/s10043-021-00679-z

Srinivasa G. Narasimhan, Mohit Gupta, Craig Donner, Ravi Ramamoorthi, Shree K. Nayar, and Henrik Wann Jensen. 2006. Acquiring scattering properties of participating media by dilution. *ACM Transactions on Graphics* 25, 3 (July 2006), 1003–1012. doi:10.1145/1141911.1141986

Baptiste Nicolet, Fabrice Rousselle, Jan Novak, Alexander Keller, Wenzel Jakob, and Thomas Müller. 2023. Recursive Control Variates for Inverse Rendering. *ACM Transactions on Graphics* 42, 4 (Aug. 2023), 1–13. doi:10.1145/3592139

Bas Nijholt, Joseph Weston, Jorn Hoofwijk, and Anton Akhmerov. 2019. Adaptive: parallel active learning of mathematical functions. doi:10.5281/zenodo.1182437

Merlin Nimier-David, Thomas Müller, Alexander Keller, and Wenzel Jakob. 2022. Unbiased inverse volume rendering with differential trackers. *ACM Transactions on Graphics* 41, 4 (July 2022), 44:1–44:20. doi:10.1145/3528223.3530073

Thomas Klaus Nindel, Tomáš Iser, Tobias Rittig, Alexander Wilkie, and Jaroslav Křivánek. 2021. A Gradient-Based Framework for 3D Print Appearance Optimization. *ACM Transactions on Graphics* 40, 4 (July 2021). doi:10.1145/3450626.3459844 Place: New York, NY, USA Publisher: Association for Computing Machinery.

James H Nobbs. 1985. Kubelka—Munk Theory and the Prediction of Reflectance. *Review of Progress in Coloration and Related Topics* 15, 1 (1985), 66–75. doi:10.1111/j.1478-4408.1985.tb03737.x

Jan Novák, Iliyan Georgiev, Johannes Hanika, Jaroslav Křivánek, and Wojciech Jarosz. 2018. Monte Carlo Methods for Physically Based Volume Rendering. In *ACM SIGGRAPH 2018 Courses (SIGGRAPH '18)*. ACM, New York, NY, USA, 14:1–14:1. doi:10.1145/3214834.3214880

Marios Papas, Christian Regg, Wojciech Jarosz, Bernd Bickel, Philip Jackson, Wojciech Matusik, Steve Marschner, and Markus Gross. 2013. Fabricating translucent materials using continuous pigment mixtures. *ACM Transactions on Graphics (TOG)* 32, 4 (2013), 1–12. Publisher: ACM New York, NY, USA.

John W. Pickering, Christian J. M. Moes, H. J. C. M. Sterenborg, Scott A. Prahl, and Martin J. C. van Gemert. 1992. Two integrating spheres with an intervening scattering sample. *JOSA A* 9, 4 (April 1992), 621–631. doi:10.1364/JOSAA.9.000621 Publisher: Optical Society of America.

John W. Pickering, Scott A. Prahl, Niek van Wieringen, Johan F. Beek, Henricus J. C. M. Sterenborg, and Martin J. C. van Gemert. 1993. Double-integrating-sphere system for measuring the optical properties of tissue. *Applied Optics* 32, 4 (Feb. 1993), 399–410. doi:10.1364/AO.32.000399 Publisher: Optical Society of America.

Michal Piovarči, Michael Foshey, Vahid Babaei, Szymon Rusinkiewicz, Wojciech Matusik, and Piotr Didyk. 2020. Towards spatially varying gloss reproduction for 3D printing. *ACM Trans. Graph.* 39, 6 (Nov. 2020), 206:1–206:13. doi:10.1145/3414685.3417850

Scott Prahl. 2011. Everything I think you should know about Inverse Adding-Doubling. (March 2011), 74. https://omlc.org/software/iad/manual.pdf

Scott Prahl. 2018. iadpython. https://github.com/scottprahl/iadpython

Scott A. Prahl. 1995. The Adding-Doubling Method. In *Optical-Thermal Response of Laser-Irradiated Tissue*, Ashley J. Welch and Martin J. C. Van Gemert (Eds.). Springer US, Boston, MA, 101–129. doi:10.1007/978-1-4757-6092-7_5

Scott A. Prahl, Martin J. C. van Gemert, and Ashley J. Welch. 1993. Determining the optical properties of turbid media by using the adding–doubling method. *Applied Optics* 32, 4 (Feb. 1993), 559. doi:10.1364/AO.32.000559

Alina Pranovich, Morten Rieger Hannemose, Janus Nørtoft Jensen, Duc Minh Tran, Henrik Aanæs, Sasan Gooran, Daniel Nyström, and Jeppe Revall Frisvad. 2024. Digitizing the Appearance of 3D Printing Materials Using a Spectrophotometer. *Sensors* 24, 21 (Oct. 2024), 7025. doi:10.3390/s24217025

Tobias Rittig, Denis Sumin, Vahid Babaei, Piotr Didyk, Alexey Voloboy, Alexander Wilkie, Bernd Bickel, Karol Myszkowski, Tim Weyrich, and Jaroslav Křivánek. 2021. Neural Acceleration of Scattering-Aware Color 3D Printing. *Computer Graphics Forum* 40, 2 (2021), 205–219. doi:10.1111/cgf.142626

Sven Schröder, Alexander von Finck, and Angela Duparré. 2015. Standardization of light scattering measurements. *Advanced Optical Technologies* 4, 5-6 (Oct. 2015), 361–375. doi:10.1515/aot-2015-0041 Publisher: De Gruyter.

Liang Shi, Vahid Babaei, Changil Kim, Michael Foshey, Yuanming Hu, Pitchaya Sitthi-Amorn, Szymon Rusinkiewicz, and Wojciech Matusik. 2018. Deep multispectral painting reproduction via multi-layer, custom-ink printing. *ACM Transactions on Graphics* 37, 6 (Dec. 2018), 1–15. doi:10.1145/3272127.3275057

Théo Phan Van Song, Christine Andraud, Luis Ricardo Sapaico, and Maria V. Ortiz Segovia. 2018. Color prediction based on individual characterizations of ink layers and print support. *Electronic Imaging* 30 (Jan. 2018), 1–6. doi:10.2352/ISSN.2470-1173.2018.8.MAAP-165 Publisher: Society for Imaging Science and Technology.

Théo Phan Van Song, Christine Andraud, and Maria V. Ortiz Segovia. 2016. Implementation of the four-flux model for spectral and color prediction of 2.5D prints. *NIP & Digital Fabrication Conference* 32 (Sept. 2016), 26–30. doi:10.2352/ISSN.2169-4451.2017.32.26 Publisher: Society for Imaging Science and Technology.

Denis Sumin, Tobias Rittig, Vahid Babaei, Thomas Nindel, Alexander Wilkie, Piotr Didyk, Bernd Bickel, Jaroslav Křivánek, Karol Myszkowski, and Tim Weyrich. 2019. Geometry-Aware Scattering Compensation for 3D Printing. *ACM Transactions on Graphics* 38, 4 (July 2019), 1–14. doi:10.1145/3306346.3322992

E. Terán, E. R. Méndez, R. Quispe-Siccha, A. Peréz-Pacheco, and F. L. S. Cuppo. 2019. Application of single integrating sphere system to obtain the optical properties of turbid media. *OSA Continuum* 2, 5 (May 2019), 1791. doi:10.1364/OSAC.2.001791

T. S. Trowbridge and K. P. Reitz. 1975. Average irregularity representation of a rough surface for ray reflection. *Journal of the Optical Society of America* 65, 5 (May 1975), 531. doi:10.1364/josa.65.000531 Publisher: Optica Publishing Group.

Philipp Urban, Tejas Madan Tanksale, Alan Brunton, Bui Minh Vu, and Shigeki Nakauchi. 2019. Redefining A in RGBA: Towards a Standard for Graphical 3D Printing. *ACM Transactions on Graphics* 38, 3 (June 2019), 1–14. doi:10.1145/3319910

Bruce Walter, Stephen R. Marschner, Hongsong Li, and Kenneth E. Torrance. 2007. Microfacet models for refraction through rough surfaces. In *Proceedings of the 18th Eurographics Conference on Rendering Techniques (EGSR'07)*. Eurographics Association, Goslar, DEU, 195–206. event-place: Grenoble, France.

Tim Weyrich, Wojciech Matusik, Hanspeter Pfister, Bernd Bickel, Craig Donner, Chien Tu, Janet McAndless, Jinho Lee, Addy Ngan, Henrik Wann Jensen, and Markus Gross. 2006. Analysis of human faces using a measurement-based skin reflectance model. *ACM Transactions on Graphics* 25, 3 (July 2006), 1013–1024. doi:10.1145/1141911.1141987

Douglas R Wyman, Michael S Patterson, and Brian C Wilson. 1989. Similarity relations for anisotropic scattering in Monte Carlo simulations of deeply penetrating neutral particles. *J. Comput. Phys.* 81, 1 (March 1989), 137–150. doi:10.1016/0021-9991(89)90067-3

Jiangping Yuan, Guangxue Chen, Hua Li, Hartmut Prautzsch, and Kaida Xiao. 2021. Accurate and Computational: A review of color reproduction in Full-color 3D printing. *Materials & Design* 209 (Nov. 2021), 109943. doi:10.1016/j.matdes.2021.109943

Tizian Zeltner and Wenzel Jakob. 2018. The layer laboratory: a calculus for additive and subtractive composition of anisotropic surface reflectance. *ACM Transactions on Graphics* 37, 4 (Aug. 2018), 1–14. doi:10.1145/3197517.3201321

Shuang Zhao, Ravi Ramamoorthi, and Kavita Bala. 2014. High-order similarity relations in radiative transfer. *ACM Transactions on Graphics (TOG)* 33, 4 (2014), 1–12. Publisher: ACM New York, NY, USA.